Small

NANO · MICRO small
www.small-journal.com

RESEARCH ARTICLE OPEN ACCESS

Suspendable and Scalable Ultrasound-Actuated ZnO-Nanosheet-Based Piezoelectric Microdevices for Wireless Electrical Stimulation of Cells

Laura Lefaix[1] | Marc Navarro[1] | Lucie Bacakova[2] | Jaume Esteve[1] | Carme Nogués[3] | Andreu Blanquer[3] | Gonzalo Murillo[1]

[1]Institute of Microelectronics of Barcelona – National Center of Microelectronics (IMB-CNM, CSIC), Carrer dels Til·lers, Campus De La Universitat Autònoma De Barcelona, Bellaterra, Barcelona, Spain | [2]Institute of Physiology of the Czech Academy of Sciences (CAS), Prague 4, Czech Republic | [3]Universitat Autònoma de Barcelona, Bellaterra, Barcelona, Spain

Correspondence: Andreu Blanquer (andreu.blanquer@uab.cat) | Gonzalo Murillo (gonzalo.murillo@csic.es)

Received: 26 September 2025 | **Revised:** 2 February 2026 | **Accepted:** 6 February 2026

Keywords: bioelectronics | cell stimulation | microdevices | piezoelectric | ZnO nanostructures

ABSTRACT

Electrical stimuli play a crucial role in activating cell signaling pathways and promoting essential functions such as migration, proliferation, and differentiation, while also enabling communication between specific cell types. Bioelectronics aims to modulate the biological activity of living tissues and organs through minimally invasive electrical stimulation. This work aims to develop and validate cytocompatible, subcellular-sized wireless microdevices fabricated through a scalable silicon microtechnology process. These microdevices consist of a micrometer-scale silicon dioxide platform integrating ZnO nanosheets (NSs) as the active piezoelectric material. They establish electromechanical interactions with cells, driven by intrinsic cellular forces or by external ultrasound actuation in the biomedical range. This study demonstrates the underpinning mechanism of this electromechanical interaction. Mechanical forces, whether generated intrinsically by cells or applied through ultrasound, deform the nanostructures and generate localized piezopotentials that depolarize the membrane and trigger calcium transients. Pharmacological studies revealed that calcium entry occurs mainly through voltage-gated calcium channels (VGCCs) and stretch-activated cation channels (SACCs), with a minor contribution from intracellular stores. Membrane potential imaging confirmed dynamic depolarization events, validating direct cell–nanogenerator coupling. Ultrasound actuation further enhanced the effect, with 58% of cells activated, underscoring the promise of piezoelectric nanogenerators for minimally invasive cellular-level bioelectronic interfaces and biomedical applications.

1 | Introduction

Current medical devices used for electrical stimulation have several limitations, that is, (i) the size and invasiveness of implantable systems; (ii) the need for a power source–wires or batteries; and (iii) the lack of spatial resolution in implantable electrodes. The use of piezoelectric materials to develop medical devices that induce an electric field to electrically stimulate cells and tissues is a novel and interesting approach that allows overcoming these limitations [1–4].

Piezoelectricity is the property of certain materials to generate a potential difference when subjected to mechanical stress, and vice versa. The piezoelectric properties depend directly on the material composition and structure. Piezoceramic materials exhibit higher piezoelectric coefficients than piezopolymers, enabling

them to generate greater electrical voltages in response to the same applied mechanical strain [5]. The main challenge of piezoceramics for biomedical applications is to find an adequate balance between biocompatibility and piezoelectric properties. For example, lead zirconate titanate (PZT) has an outstanding piezoelectric performance and is cost-effective, but it is highly cytotoxic to cells [6].

Piezoelectric devices based on PZT have been miniaturized to millimeter (1.7 mm^3) and submillimeter (0.1 mm^3) scales, enabling tissue-level spatial resolution [7, 8]. In contrast, the use of piezoelectric nanomaterials can offer single-cell spatial resolution, but their size, much smaller than that of a typical cell (tens of μm), makes them difficult to manipulate. As a result, they generally lack the ability to perform complex bioelectronic functions and are often internalized by the cell [9, 10].

Complementing these material-based strategies, ultrasound actuation has emerged as an effective method for controlled wireless energy delivery and non-invasive stimulation in bioelectronics. Ultrasound has been explored in diverse biomedical contexts, including neuromodulation and wound healing [11, 12], and it can be used for activating piezoelectric materials [7, 13], underscoring its potential as a versatile tool for next-generation implantable and wearable devices.

Several studies have demonstrated that piezoelectric stimulation can modulate cellular activity across different cell types. These effects include enhanced calcium signaling [9, 14], upregulation of differentiation markers [15, 16], and improved functional responses [17], highlighting the versatility of piezoelectric platforms for applications in bone regeneration [15, 16], neuromodulation [13, 18], and muscle stimulation [4, 7].

A wide variety of cell types can react to electrical stimuli. These cells can be classified as excitable and non-excitable. The difference between them is the production of action potentials, a specific membrane depolarization due to a rapid sequence of changes in the voltage across the cell membrane [19]. In excitable cells, such as neurons, action potentials are a means of cell communication, or initiate specific cell functions, such as muscle cell contraction [20–22]. By contrast, in non-excitable cells, such as epithelial cells, chondrocytes and osteoblasts, the electrical signaling induce slower changes in the voltage across the membrane, the effect of which would trigger the activation of several cellular pathways leading to cell migration, proliferation, differentiation and even cell death [19, 23].

Among non-excitable cells, osteoblasts are a well-established model to study cell electrical stimulation. In osteoblasts, it has been proposed that exposure to an electric field induces a gradient in the electric potential of the membrane that, in turn, affects ion fluxes asymmetrically, playing a critical role in controlling Ca^{2+} flux [24, 25]. Furthermore, it has been reported that electric fields in the range of 10 V cm^{-1} or higher induce intracellular calcium elevation in osteoblasts [25–27]. Ozkucur et al. deduced that voltage-gated calcium channels (VGCCs) in the cell membrane play a key role in this process in Saos-2 osteosarcoma cells, depending on the field intensity [25]. In osteoblasts, VGCCs are implicated in several functions [19], such as the increase of bone tissue formation [28], bone mineralization [29], and hormone secretion [19].

As previously mentioned, osteoblasts are non-excitable cells that are able to respond to electric fields. Under physiological conditions, osteoblasts are subjected to piezoelectric stimulation due to the piezoelectric nature of the bone [6, 30–32]. Understanding the interplay between bone cells and their matrix is crucial, as leveraging the benefits of microscale interactions and nanoscale piezoelectricity. In this context, piezoelectric ceramics have emerged as promising biomaterials for orthopedic applications. They enable self-powered electrical stimulation from in situ mechanical energy sources such as body motion or inherent cell forces [14]. Furthermore, these materials allow for wireless actuation via externally-applied ultrasound, broadening their potential for minimally invasive and remote biomedical applications [16, 33].

Among all piezoceramics, ZnO has gained much interest in the biomedical field. ZnO nanostructures in the form of nanosheets (NSs) have been thoroughly tested in our group for potential biomedical applications. Previous works by our group deeply studied and characterized ZnO NSs as a piezoelectric material [14, 34, 35]. The piezoelectric performance of ZnO NSs, with a piezoelectric coefficient (d_{33}) of 4–6 pm V^{-1} [14], is well-balanced with the material's biocompatibility. This is due to the fact that ZnO is a crystalline material composed of zinc and oxygen, elements that are naturally found in the human body, although zinc exists only in trace amounts. It has been shown that the Zn^{2+} ions released by ZnO NSs in culture throughout 21 days did not have any cytotoxic effect on muscle cells [36]. Although ZnO exhibits a lower piezoelectric coefficient compared to PZT and $BaTiO_3$, its performance is sufficient to generate the electrical stimulus required for effective cell modulation. In addition, its inherent biocompatibility makes ZnO a safer alternative for biomedical applications involving direct interaction with biological tissues.

The objective of the work presented here is to demonstrate the use of a cytocompatible piezoelectric microdevice, fabricated through micro- and nanotechnology processes, and able to wirelessly stimulate single cells through the generation of local electric fields. Microfabrication techniques enabled the production of silicon microparticles, microscale platforms smaller than a typical human cell, used as substrates for the hydrothermal growth of piezoelectric ZnO nanostructures, synthesized as randomly oriented NSs. These ZnO NSs, with a thickness of a few nanometers, can be activated by pressure waves within the biomedical ultrasound range. The reduced dimensions enhance cell–microdevice interaction and improve the stimulation spatial resolution. While the design has been intentionally simplified to facilitate fabrication and integration, the use of advanced microfabrication techniques ensures that more complex circuits and electronic components can be incorporated in future versions. The current design is better suited to enable subcellular-scale electrical stimulation, electromechanical cell interaction, and cell-interfacing investigations, providing essential insights that can guide future development of advanced, functional devices, rather than serving as a fully programmable or implantable

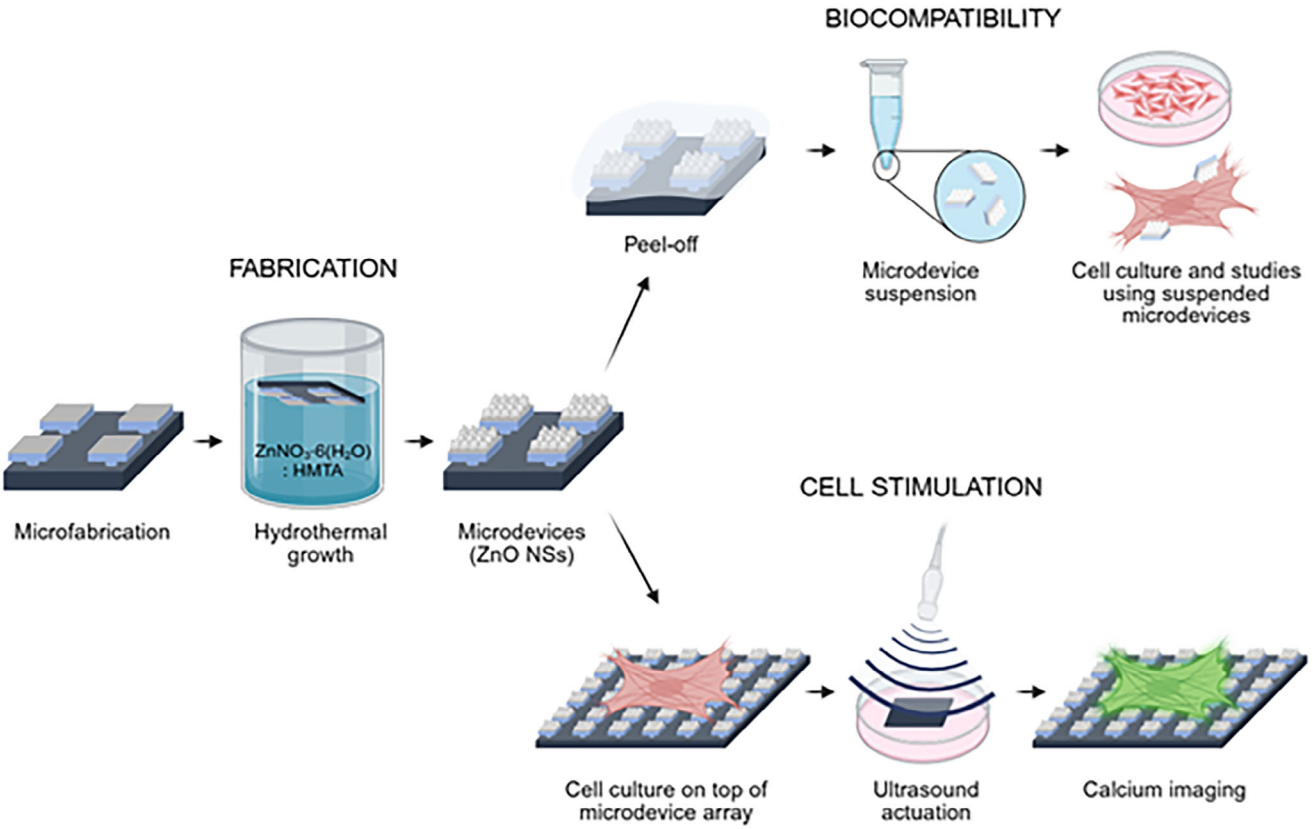

FIGURE 1 | Fabrication process and application of the microdevices to cell cultures. First, the core microparticles were produced by microfabrication, inspired by previous works [37]. Then, ZnO nanosheets (NSs) were grown on the microparticles by hydrothermal growth to form the final microdevices. Some of the microdevices were peeled off from the support wafer, suspended in water, and sterilized, following a patented process [38], and then added to the cell culture for a cytocompatibility evaluation. On the other side, microdevices anchored to the silicon wafer (i.e., not released) were used to test, via calcium imaging, the effect of the electrical stimulation generated by the piezopotential on the ZnO NSs after being actuated with ultrasound.

bioelectronic system at this stage. Thus, this study aims to demonstrate cell stimulation by measuring the increase in intracellular calcium. Saos-2 cells were chosen as a simplified model due to their reproducible characteristics of generating calcium transients in response to an exogenous electric field [14, 25]. Furthermore, the source of calcium was analyzed to determine whether it originates from extracellular influx through VGCCs, SACCs or from intracellular stores, such as the endoplasmic reticulum. This comprehensive analysis provides insights into the mechanisms of cellular response to piezoelectric materials.

2 | Results and Discussion

Microdevices were first designed as 3 μm x 3 μm microparticles [37], later covered with uniform ZnO NSs grown over a selective area using a low-cost, mild-temperature, and reproducible hydrothermal method. The microdevices were characterized and evaluated using osteoblast cultures, either after being released from the silicon wafer, allowing assessment of their cytotoxicity and interaction with cells in suspension, or while remaining attached to the wafer in an array configuration to investigate their ability to electrically stimulate osteoblasts. Figure 1 illustrates the piezoelectric microdevice fabrication process and the in vitro studies performed.

2.1 | Microdevice Fabrication and Characterization

The microfabrication process involved four key steps (Figure 2A): (i) deposition of aluminum nitride (AlN), (ii) photolithography, (iii) reactive ion etching (RIE) to define the microparticle geometry, and (iv) wet etching to form the underlying pillars. A 100 nm-thick AlN layer, deposited using radio frequency (RF) reactive sputtering, was used as a catalyst layer for the hydrothermal growth of the ZnO NSs [35, 39]. Subsequently, a 1.2 μm-thick positive photoresist was applied for the photolithography process. A photomask containing discrete 3 × 3 μm^2 squared patterns was used to define the microparticle outlines. RIE of the AlN and SiO_2 layers was then performed to define the microparticle structures. Finally, partial wet etching of the SiO_2 beneath the patterned microparticle resulted in the formation of well-defined microparticle pillars [37].

The microparticle morphology was examined by scanning electron microscopy (SEM). The microparticles on the wafer showed good homogeneity as well as correct formation of the standing pillar for an appropriate subsequent peel-off step. The microparticles obtained after the process had a final size of 3.4 ± 0.1 μm (Figure 2C, Figure S1). The shape of the microparticle is equally important. A square was selected because it was simple to

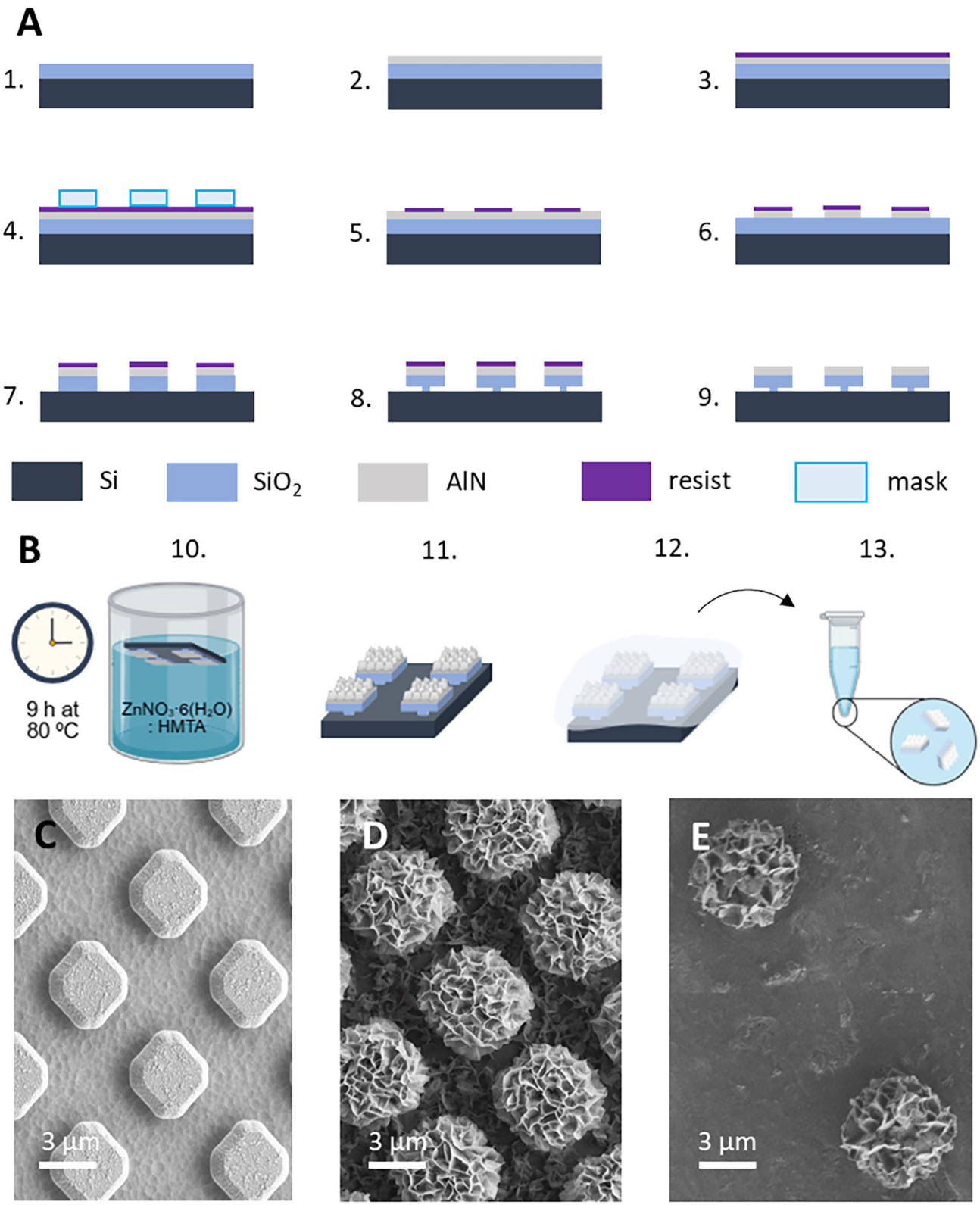

FIGURE 2 | Microfabrication process of microdevices. (A) Scheme of the successive steps of the microfabrication process: oxidation (1), sputtering of the AlN layer (2), photoresist spin coating (3), photolithography (4), resist development (5), dry etching of the AlN layer (6), SiO_2 dry etching (7), wet etching to create the pillar of the microparticle (8), and resist stripping (9). (B) Hydrothermal growth of ZnO nanostructures for 9 h at 80°C in a $ZnNO_3$:HMTA solution (10), resulting in the final microdevices attached to the wafer through thin pillars (11). Peeling-off of the microdevices (12), followed by polymer dissolution to obtain individual suspended microdevices through a patented process (13) [37, 38]. (C) SEM image of the fabricated microparticles (tilted at 45°). (D) SEM image of the microdevices after the hydrothermal growth step. (E) SEM image of the released microdevices.

fabricate, easy to detect in microscopy inspections, and serves as a stable template for ZnO NSs growth. Other studies have shown that more complex morphologies, such as star-shaped microparticles, can induce cell death [40], which is counterproductive for our goal of biocompatible cell stimulation. The microfabrication process described can be readily adapted to larger-scale production by utilizing foundry-level techniques with larger wafers, enabling the fabrication of billions of microdevices per batch.

Piezoelectric ZnO NSs were grown on top of the microparticles (Figure 2B,D) [35, 41]. The final thickness of the top layer created by the forest of ZnO NSs was around 1 μm after the hydrothermal synthesis. The overall size of the final microparticles covered by the ZnO NSs was 4.9 ± 0.3 μm (Figure S1). We define a "microdevice" as the combination of a microparticle covered by piezoelectric ZnO NSs [42]. The overall surface of the microdevices is around 25 μm^2, giving them the right size to interact with a single cell. Millions of microdevices were obtained per wafer fabricated [43].

As recently demonstrated, the NS length and thickness depend both on the chemical synthesis duration and the thickness of the deposited aluminum-based layer [39, 42]. After 9 h of growth, the hydrothermal synthesis resulted in homogeneous distribution of randomly-oriented NSs, uniformly covering the top surface of the microdevices. The mean value of the NS thickness was 21 ± 4 nm. The selected hydrothermal synthesis was optimized to offer a good balance among synthesis efficiency, piezoelectric response and electromechanical performance [42]. In addition, concerning the ZnO nanostructure shape, growing NSs was preferred over nanowires (NWs), as NWs have the potential to pierce the cell membrane, leading to cellular damage. Since cells tend to prefer smoother and flatter surfaces, NSs facilitate a better cell-material interaction and reduce the risk of membrane disruption.

To release the devices from the wafer surface, they were peeled off and suspended in ethanol for storage and forthcoming use (Figure 2B,E) [37]. It was calculated that 82% of the microdevices were recovered for further studies after the process. The microdevices were dispersed evenly in the cell culture medium without forming clusters, and the suspension of microdevices remained homogeneous with minimal intervention. The presence of ZnO NSs grown on the microdevices is suggested to drastically reduce the tendency for aggregation [44, 45]. Additional supplementary characterization of the microdevices can be found in Figure S1.

Silicon microfabrication techniques offer precise control over the size, shape, and surface properties of microdevices. This design flexibility marks a key advantage over commercial piezoelectric micro- and nanoparticles.

2.2 | Electrical Characterization of an Array of ZnO NSs

Electrical characterization of ZnO NSs was previously performed by our group. The piezoelectric coefficient of the ZnO NSs showed d_{33} values of 4–6 pm V^{-1} [14, 34, 35]. Additional piezoelectric performance of ZnO NSs is assessed in the mentioned publications. Here, to evaluate the electrical performance of the piezoelectric NSs in response to ultrasound, an epoxy-embedded piezoelectric test device was fabricated and exposed to an acoustic wave with a frequency of 3 MHz and different intensities (0.2, 0.6, 1, and 2 W cm^{-2}). The test device was composed of ZnO NSs sandwiched between a platinum (Pt) top electrode with a zigzag profile and a molybdenum (Mo) bottom electrode. The setup is depicted in Figure S2. The voltage measured between both electrodes, in the range of millivolts, was directly proportional to the intensity of the acoustic wave and is produced by the ZnO NS piezopotential (Figure 3). A greater intensity induces a larger strain in the piezoelectric nanostructure, thus generating a greater piezopotential.

For 0.2 W cm^{-2} intensity, the peak-to-peak signal voltage obtained was 0.8 ± 0.1 mV. In addition, 1.3 ± 0.1 mV was measured for 0.6 W cm^{-2}, 1.6 ± 0.1 mV for 1 W cm^{-2}, and 3.1 ± 0.3 mV for 2 W cm^{-2}. These voltage measurements were obtained after applying a digital low-pass filter computed in MATLAB. In the original signals, a ripple could be observed (Figure 3B) with peak-to-peak amplitudes of 0.6 ± 0.3, 0.8 ± 0.3, 0.9 ± 0.3, and 2.1 ± 0.3 mV for 0.2, 0.6, 1, and 2 W cm^{-2} acoustic intensities, respectively.

It is difficult to quantitatively extrapolate these measurements to the system later used to stimulate cells due to the change in the acoustic medium, from the polymer-embedded test device with ZnO NSs to the microdevices in an aqueous medium. However, this measurement is useful to validate the expected piezoelectric response of the microdevices when actuated with ultrasound.

2.3 | The Effect of Microdevices and Acoustic Waves on Osteoblast Viability

Our group has demonstrated that ZnO NSs, whether adhered in a large area [14, 15, 36], or as part of individual suspended microdevices [42], are non-cytotoxic. Even though the biocompatibility of the microdevices has been proven, we have analyzed the interaction between Saos-2 cells and the microdevices as well as the safety of the method used to actuate them (i.e., ultrasounds). The addition of 2:1 microdevices/cells allowed obtaining a favorable proportion for the final interaction in culture. Figure 4A shows the results for the viability of microdevices after 1, 3, and 7 days in culture. As expected, results demonstrated the microdevices were cytocompatible according to ISO 10993–5 [42]. Although on day 3, the viability of cells cultured in the presence of microdevices was reduced, this was by less than 30%, which is the limit for a material to be considered cytotoxic according to the ISO 10993–5 standard. Furthermore, on day 7, cell viability returned to a level comparable to that of control cells without microdevices. Figure 4B shows that 49% of the cells had one microdevice in contact. A decreasing trend in the number of cells with several attached devices was evident, showing a tendency toward having one or two microdevices per cell (i.e., 75% of cells). The interaction between the microdevices and the cells, as well as their relative position, was analyzed using SEM (Figure 4C). In addition, confocal laser scanning microscopy was performed to corroborate the results (Figure S3). The preferred orientation for the electrical stimulation of the cell is with the microdevices positioned so that the NSs face the cell membrane. This configuration maximizes intimate contact between the deformed NSs and the cell membrane, which helps to prevent charge compensation or screening by mobile charges in the extracellular medium, and

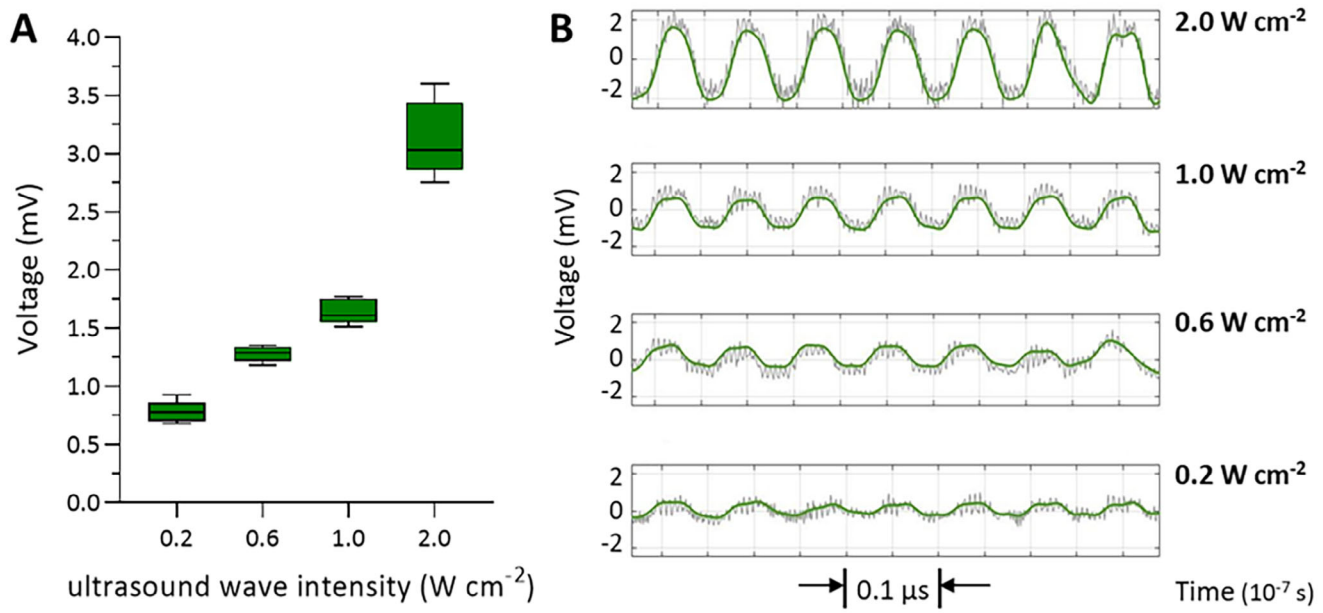

FIGURE 3 | Electrical characterization of an epoxy-embedded test device composed of ZnO NSs sandwiched between electrodes actuated by an ultrasound wave of a frequency of 3 MHz and different intensities (0.2, 0.6, 1, and 2 W cm^{-2}). (A) Graph of the peak-to-peak voltage measured for different ultrasound intensities. (B) Transient voltage measurements of the filtered signal (green) versus the original signal (gray). Data are expressed as mean ± SD from five independent measurements (n = 5).

enhances the effect of the local electric field generated by the piezopotential resulting from the NS deformation. In the current version of the system, the orientation of individual microdevices cannot be actively controlled. In future applications, the NSs will be functionalized to enable active guidance and control of the microdevice orientation.

We propose the use of ultrasound to wirelessly actuate the ZnO NSs integrated in the microdevices. The range of biomedical ultrasound generally used goes from 1 to 20 MHz and ensures the safety of ultrasound crossing the biological tissue without damaging the organism [46–48]. 1.0 W cm^{-2} is close to the maximum limit of ultrasound intensity recommended by the Food and Drug Administration (FDA) [49]. Nevertheless, the American Institute of Ultrasound in Medicine published an extensive study questioning these generalized values [50], highlighting the importance of testing the ultrasound conditions specifically for each study to verify accuracy. Therefore, to exclude any negative effect of the applied ultrasound on cell viability, Saos-2 cells were exposed to an acoustic wave of 3 MHz in the presence and absence of microdevices and evaluated 24 h after exposure.

Ultrasound was applied three times for 10 s, each 5 min, at three different intensities, that is, 0.2, 0.6, and 1.0 W cm^{-2} (Figure S4). No changes in culture temperature derived from this actuation were observed. The results for cell viability are shown in Figure 4D,E. For each intensity tested, cell viability was above 90%. No statistically significant differences were found between cells exposed to ultrasound in the presence or absence of microdevices at any intensity tested, with the exception of 0.6 W cm^{-2}. This suggests the possibility of some damage to the cell membrane by ultrasound; however, the overall viability of the cells decreased only slightly, and not by 30%, which is the limit of harmful effects according to the ISO 10993-5 standard. Cell viability for ultrasound actuation at 1 MHz was also tested and can be found in Figure S5.

The evaluation of the microdevices after ultrasound application revealed no changes in either the surface morphology or the attachment of the ZnO NSs to the silicon substrate (Figure S6). This suggests that microdevices are structurally robust under the ultrasound conditions applied.

It can be concluded that neither the microdevices nor the method used to actuate them is cytotoxic for Saos-2 cells. The hybrid architecture of the microdevice, comprising ZnO nanostructures anchored onto a silicon microparticle, leverages the microscale dimensions of the core, while preserving the nanoscale properties of the ZnO NSs. The use of microdevices results in an important reduction of the exposed ZnO surface, minimizing the possible cytotoxicity of nanostructured ZnO. Moreover, the stability of the microdevices and the ZnO NSs was demonstrated. The microdevices are structurally robust and capable of withstanding the application of ultrasound without degradation. Once proved that cell viability remained unaffected by the ultrasound actuation, the next step was to validate and evaluate the ability of the actuated microdevices to stimulate cells.

2.4 | Mechanism of Intracellular Calcium Activation in Response to ZnO NSs

Again, Saos-2 cells were selected as a simplified osteoblast model to elucidate the effect of ZnO NSs on cell behavior. Saos-2 cells show a reproducible ability to generate calcium transients—temporary increases in intracellular calcium ion concentration—in response to an exogenous electric field. These cells have previously been used to assess cellular responses to

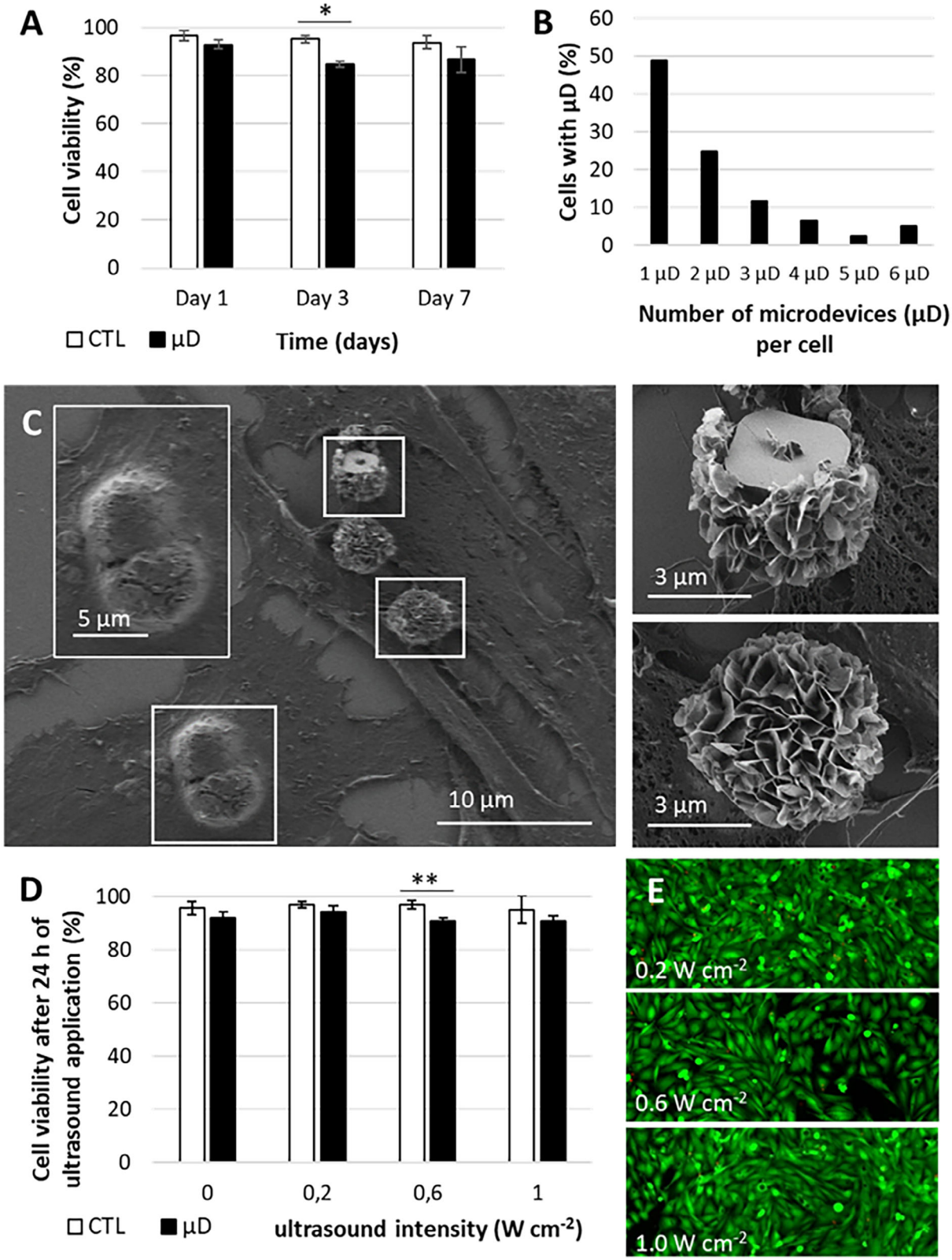

FIGURE 4 | Cell viability and microdevice (µD) position. (A) Cytocompatibility of Saos-2 cells without (CTL) and with microdevices (1:2) after days 1, 3, and 7 of cell culture. (B) Percentage of cells with different numbers of microdevices (1 to 6) in contact. A total of 323 cells were counted. (C) SEM image of cells in contact with several microdevices. Zoom (insets) of different sections of the image showing the three different positions that were taken. (D) Cytocompatibility of Saos-2 cells in absence (CTL) and presence of microdevices (µD) after 24 h of exposure to three cycles of 10 s of ultrasound actuation separated by a 5 min period of relaxation. Three different intensities are represented (0.2, 0.6, and 1.0 W cm^{-2}) at an ultrasound frequency of 3 MHz. E) Cell viability images of a sample with microdevices, exposed to ultrasound at 3 MHz and three different intensities (0.2, 0.6, and 1.0 W cm^{-2}). Data are expressed as mean ± SD from three independent experiments (n = 3). Student's t-test was used to assess differences; asterisks (*) indicate significant differences at $p < 0.05$.

electrical stimulation via calcium imaging in several studies [14, 25, 51]. Indeed, calcium imaging is a common, straightforward technique performed for the evaluation of stimuli-responsive materials [13, 18].

In this experiment, microscopic glass coverslips with ZnO NSs grown on their surface were used to study Saos-2 cell activation through calcium imaging. Our aim was to establish a more comprehensive model of cell activation, based on previous knowledge, and analyze the different contributions that lead to changes in the cytoplasmatic Ca^{2+} concentration. Previous studies demonstrated that mechanical forces exerted by Saos-2 cells upon adhesion to the ZnO nanostructured substrate generate a local electric field arising from the piezoelectric potential of mechanically deformed ZnO NSs, thereby promoting self-stimulation and influencing cellular behavior [14]. The increase in intracellular Ca^{2+} concentration in osteoblasts can be triggered by several routes. The three main mechanisms proposed to explain the intracellular Ca^{2+} concentration increase act either externally, that is, via the opening of (i) VGCCs or (ii) stretch-activated cation channels (SACCs) located in the plasma membrane, or internally, that is, (iii) via the opening of calcium ligand-gated channels located on the endoplasmic reticulum. Ca^{2+} serves as a second messenger in numerous pathways that can regulate the proliferation and differentiation of osteoblasts, specifically, or cells, in general (Figure 5A) [14, 52].

To elucidate the mechanisms involved in this increase, we performed a set of experiments to measure intracellular calcium transients in Saos-2 cells grown on ZnO NSs and glass coverslip (control). Cells were cultured under the following conditions: (i) in standard cell culture medium, (ii) in calcium-free Hanks' balanced salt solution (HBSS), (iii) in the presence of nifedipine or (iv) in presence of gadolinium. In these experiments, no external actuation was used to strain the NSs, but the inherent forces exerted by the cells on the ZnO NSs.

First, we aimed to elucidate on the origin of the Ca^{2+} ions responsible for the influxes. To achieve this, we compared the number of excited cells grown in the presence or absence of Ca^{2+}. The percentage of cells presenting calcium transients under standard conditions (i.e., cultured in a medium containing Ca^{2+}) was 3.5 times higher in cells cultured on ZnO NSs than on those cultured on control glass, with values of 51% versus 14%, respectively. When calcium-free HBSS was used, the percentage of excited cells decreased to 13% in cells grown on ZnO NSs and to 5% in cells grown on control glass. This demonstrated that 75% of the calcium transients originate from the extracellular medium in cells cultured on ZnO NSs.

Next, we studied the role of different types of calcium channels, VGCCs and SACCs, in the generation of Ca^{2+} influxes. To achieve this, we used two different calcium channel blockers: gadolinium and nifedipine. Gadolinium is known to primarily block SACCs, although some studies have also shown that it can block VGCCs [53]. Nifedipine, on the contrary, is a well-established VGCC blocker. Gadolinium reduced the number of excited cells to 9% in control cultures and 20% in cells grown on ZnO NSs. Conversely, nifedipine reduced the number of excited cells to 11% and 33% in control and ZnO NS cultures, respectively (Figure 5B). The video recording of the time-lapse experiments can be found in Movie S2, where the reduction in the calcium influxes can be observed.

Taking all these results together, it is possible to hypothesize that the forces exerted by the cells on the ZnO NSs induce local electric fields capable of opening the two different calcium channels present in the cell membrane. According to Khatib et al., VGCCs require an electric field above 10 V cm^{-1} to open, whereas only 2 V cm^{-1} is sufficient to open SACCs [26]. The force exerted could vary depending on factors such as cell size, movement, or the distance of cell prolongations on the NSs. Consequently, the piezopotential generated may selectively open either VGCCs or SACCs. Additionally, there is a percentage of excited cells in the absence of Ca^{2+} outside of the cell; in this case, we suggest that calcium transients are originated from internal calcium stores mediated by electrical stimulation-induced phospholipase C (PLC) activation [26, 54]. Our results reveal that the mechanism which triggers the increase in intracellular Ca^{2+} concentration involves multiple entry routes.

To further confirm that a local electrical field is generated when cells exert forces on the NSs, a voltage-sensitive probe, that is, $DiBAC_4(3)$, that measures changes in membrane potential, was employed. The results consistently showed higher depolarization levels in cells seeded on top of ZnO NSs at the beginning of the time-lapse experiment. This depolarization is not observed in control samples. Beyond this, throughout the entire recording, between 55% to 70% of cells cultured on ZnO NSs exhibited dynamic changes in the membrane potential, observed by fluctuations in fluorescence intensity (Figure 5C, Movie S3). In control samples, these cells are below 14%. The mentioned percentages are consistent with the subsets of cells that present intracellular calcium transients, respectively.

2.5 | Cell Stimulation Through Actuation of Microdevices

To analyze the ability of the microdevices to electrically stimulate osteoblasts in response to ultrasound actuation, an array of microdevices attached to a silicon wafer was used. In these experiments, the microdevices were not released from the silicon chip but instead remained attached to it, ensuring that the ZnO NSs were in direct contact with the cell membrane.

Electrical stimulation was analyzed in terms of the presence of calcium transients in the Saos-2 osteoblasts. We expected to observe changes in the intracellular Ca^{2+} levels in cells grown on ZnO NSs compared to the control cells, due to the local electric field induced by the piezoelectric ZnO NSs when actuated by ultrasound at a frequency of 3 MHz.

The results obtained are depicted in Figure 6. Three different conditions of wave intensity were tested: (i) 0.2 W cm^{-2}, (ii) 0.6 W $cm^{-2,}$ and (iii) 1.0 W cm^{-2}. Ultrasound was applied three times sequentially for 10 s, each 5 min (Figure S4).

The percentage of excited cells was quantified in the absence of ultrasound (basal stimulation), and after each cycle of ultrasound actuation (first, second, and third cycles) (Figure 6A). At 1.0 W cm^{-2}, the basal cellular excitation level was 22% and after the

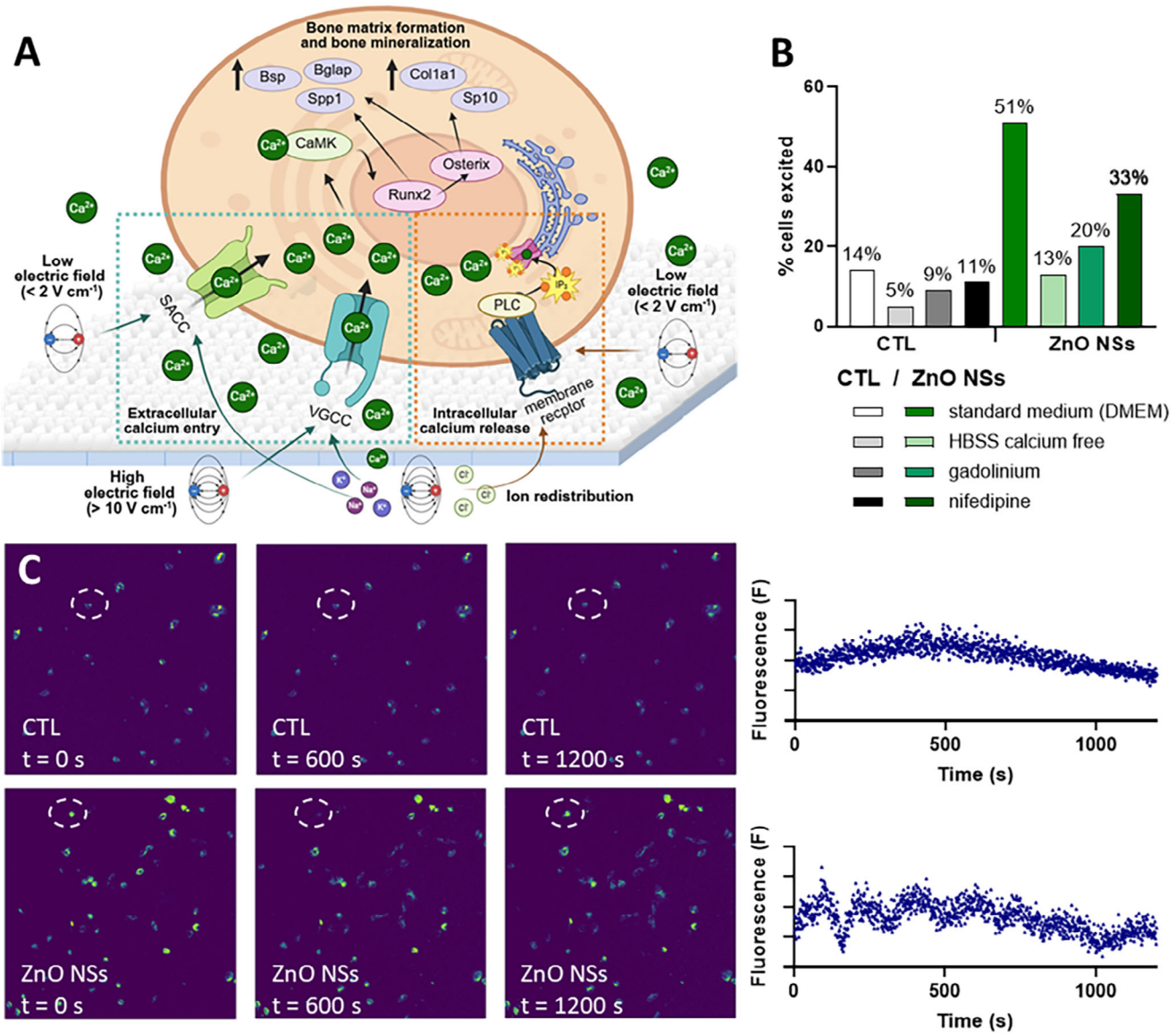

FIGURE 5 | Ca^{2+} influx routes, activated in Saos-2 cells cultured on ZnO NSs. Different entry routes responsible for intracellular calcium transients are depicted in (A). The Ca^{2+} origin can be intracellular, where the external stimuli are transduced through membrane receptors, or extracellular, by opening either voltage-gated calcium channels (VGCCs) or stretch-activated cation channels (SACCs) depending on the intensity of the exogenous electric field. The graph in (B) shows the percentage of cells excited when cultured on ZnO NSs compared to control (CTL) glass coverslips in different conditions: HBSS (Ca^{2+} free), gadolinium (SACC blocker) or nifedipine (VGCC blocker). Excited cells exhibited at least one event of fluorescence intensity exceeding a 5-fold increase over the basal signal during the 15-min time-lapse recording. The progression of images in (C) shows cells stained using $DiBAC_4(3)$. Most of the cells of the ZnO NS samples exhibit early activation compared to control cells, which show lower fluorescence intensity. In addition, the cell membrane potential remains stable in control, while in the ZnO NS samples some of the cells undergo changes in their membrane potential during the recording, as indicated by the graphs showing the fluorescence intensity during the time-lapse experiment. Data are expressed as counts from three independent experiments (n = 3).

first cycle of ultrasound actuation the percentage of excited cells increased to 35%. The percentage of excited cells after the second and third cycles of ultrasound actuation, although slightly reduced, continued to be above 30%. However, no significant differences were observed when the same intensity was applied to the control cells (Movie S4).

In the case of the samples actuated at 0.6 W cm^{-2}, a significant increase in the percentage of excited cells was observed after the first stimulation in both the control cells and the cells in contact with the microdevices. However, this effect was much more pronounced in cells in contact with microdevices, doubling the percentage of excited cells (from a basal 14% to 28% after the first ultrasound actuation). However, after the second and third actuation, the percentages of cells excited in contact with microdevices were not as high as for the first actuation.

Finally, in samples in contact with microdevices actuated at an intensity of 0.2 W cm^{-2}, a slight increase in the percentage of

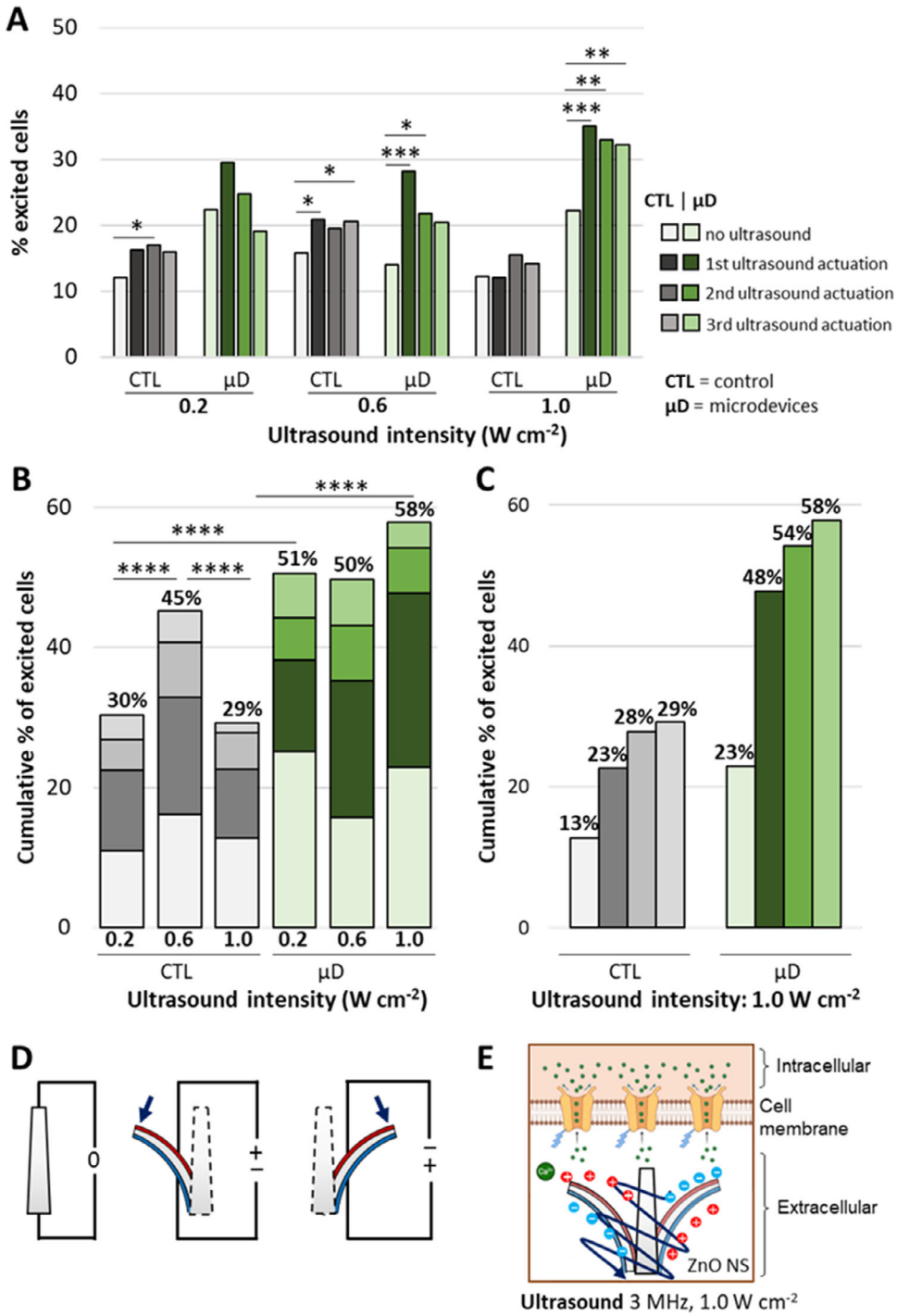

FIGURE 6 | Effect of microdevices in Saos-2 cell stimulation. (A) Percentage of excited cells in control (CTL) samples, without microdevices, and samples with microdevices (μD) for ultrasound actuation at 3 MHz and three different intensities (0.2, 0.6, and 1.0 W cm^{-2}) for three consecutive cycles of 10 s followed by a resting time of 5 min (no ultrasound, first stimulation, second stimulation and third stimulation). Excited cells exhibited at least one event of fluorescence intensity exceeding a 5-fold increase over the basal signal during the 5-min time-lapse recording after each actuation. (B) Total percentages of excited cells after the three stimulation rounds according to the nomenclature in (A). Cell excitation was quantified similarly to the previous 18-min time-lapse analysis, accounting for cumulative effects throughout the entire recording period. (C) Cumulative percentage of cells excited after each ultrasound actuation at 1.0 W cm^{-2}. (D) Piezoelectric effect in the ZnO NSs in response to the mechanical stress induced by ultrasound actuation (blue arrow). (E) Scheme of the hypothesized mechanism of Ca^{2+} entry induced by the presence of ZnO NSs. The generated piezopotential in the ZnO crystalline structure, in response to a mechanical stimulus, is responsible for inducing a local electric field close to the cell membrane which triggers the opening of VGCCs. Data are expressed as counts from three independent experiments (n = 3). Chi-square test was used to assess differences; asterisks (*) indicate $p < 0.05$.

excited cells can be perceived (30%), but no significant differences were observed between stimulated and non-stimulated samples.

More importantly, when considering the total percentage of cells excited after the three cycles of ultrasound actuation (Figure 6B), significant differences were observed. The percentage of stimulated cells nearly doubled when the control cells were compared to the cells that were cultured on top of the microdevices. Specifically, the percentage increased from 30% (control) to 51% (microdevices) at 0.2 W cm^{-2}, and from 29% (control) to 58% (microdevices) at 1.0 W cm^{-2}. However, the basal cellular excitation level was higher for control cells at 0.6 W cm^{-2} compared to the other two stimulation intensities. At this intensity, no significant differences were found between control cells (45%) and cells grown on microdevices (50%). Cumulative percentages of cells excited after each ultrasound actuation at 1.0 W cm^{-2} are detailed in Figure 6C.

As first demonstrated by Murillo et al. [14], and corroborated in this work, the forces exerted by the cell on a piezoelectric ZnO NS seem to be sufficient to produce a local electric field and an associated ion redistribution that triggers some membrane calcium channels, inducing an increase in intracellular calcium in cells responding to the stimulus.

We hypothesize that the increase in the percentage of excited cells observed in the control samples at 0.6 W cm^{-2} could be due either to ion transport or to the opening of SACCs, both triggered by the ultrasound wave. Conversely, in cells in contact with microdevices, the increase in the percentage of excited cells could be due to a combination of the opening of both channels, SACCs and VGCCs, triggered by the piezoelectric potential generated in the ZnO NSs by the ultrasound actuation (Figure 6D and Figure 6E).

In addition, changes in the calcium transient patterns were also observed. We suggest that this effect could also be related to the different calcium channels activated. More information can be found in Figure S7.

Changes in the intracellular Ca^{2+} concentration induce different cellular responses [55, 56]. Although this work does not focus on the osteogenic capability, the effect of these changes on cellular behavior, due to the interaction of osteoblast-like cells with ZnO NSs, was previously studied by our group. Saos-2 cells grown on ZnO NSs showed increased proliferation after 7 days in culture and an increase in osteogenic markers of bone matrix formation and bone mineralization after 21 days [15]. The increase in intracellular Ca^{2+} could lead to an increase in cell activity, which would eventually cause the switching on or off of cellular processes [56], affecting cell proliferation or differentiation.

2.6 | Finite Element Modelling Simulations in COMSOL

Simulations based on finite element modelling (FEM) were performed to estimate the intensity of the electric fields generated by a single ZnO NS in the surroundings of the cell membrane, when actuated by an ultrasound wave at a frequency of 3 MHz.

Figure 7 shows the electric field produced by a single ZnO NS close to the cell membrane in response to ultrasound. Two models have been considered: (i) whether the end of the ZnO NS is free to move (Figure 7A), modelled at a distance of 5 nm from the cell membrane, or (ii) when it is embedded within the membrane (Figure 7B). To ensure computational feasibility while capturing the essential behavior, the model incorporates simplified assumptions, such as idealized cell–nanosheet contact geometries and single-nanosheet configurations. Since the real scenario likely falls between these two extremes, the simulated electric field values can be interpreted as theoretical lower and upper bounds, providing an estimated range rather than an exact quantitative prediction of the experimental system.

The intensity distribution of the electric field at the higher intensity applied (1.0 W cm^{-2}) is depicted in the images. A cross-section of a ZnO NS in contact with the cell membrane and the magnitude of the electric field generated along the x–z plane is presented for both models. Complementarily, an x-y plane view of the modelled cell membrane shows the significant magnitude of the electric field produced by the ZnO NS in the vicinity of the membrane. The area of interest of the membrane affected by the electric field extends beyond the ZnO NS in both cases. In any case, the electric field intensity generated by the embedded NS is much higher than in the case of the free-end NS.

Figure 7C shows how the acoustic wave of 3 MHz and 1.0 W cm^{-2} travels through the aqueous medium and reaches the ZnO NS. Figure 7D depicts the deformation produced in the ZnO NS by this wave, as schematized in Figure 6E. The three different acoustic intensities used for the cell excitation experiment (0.2, 0.6, and 1.0 W cm^{-2}) were replicated for the simulations. The resulting maximum electric field intensities are shown in Figure 7E. The embedded ZnO NS produces an electric field intensity that is two orders of magnitude higher than that produced by the free-end NS, ranging between 10^3 to 10^4 V cm^{-1}, or 10^0 and 10^2 V cm^{-1}, respectively. The magnitude increases with the intensity of the acoustic wave, due to a higher strain produced in the ZnO NSs.

A movie comparing the resulting acoustic pressure at the ZnO NSs-cell membrane system, the deformation of the ZnO NSs in response to this acoustic pressure, and the electric field produced due to this deformation can be found in Supporting Information (Movie S5).

Considering that an electric field above 10 V cm^{-1} induces calcium transients in the cells by triggering VGCCs [26, 27], a partially embedded ZnO NS should be capable of triggering the opening of VGCCs since the intensity of the produced electric field is higher than this value.

This simulation was designed based on the average size of the ZnO NSs grown on the microdevices. Nevertheless, the parametric study shown in Figure S8, allowed us to understand how the NS diameter and thickness affect its resonance frequency. As expected, the thinnest and largest ZnO NS exhibits the lowest resonance frequency. These dimensions can be tuned by varying the hydrothermal growth conditions [35, 39, 42], resulting in an effective way of modulating the electrical response of the piezoelectric nanostructures in response to the ultrasound wave

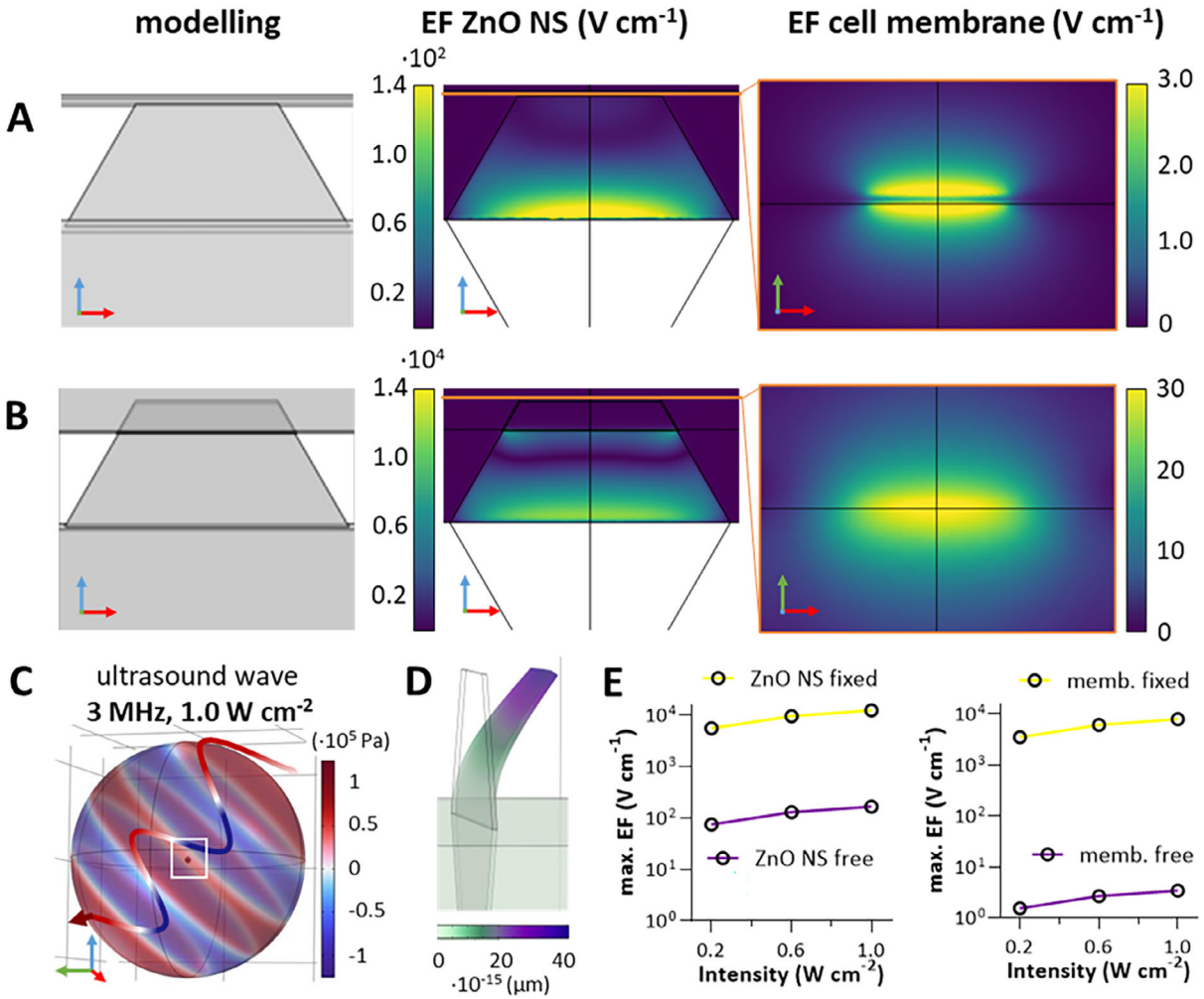

FIGURE 7 | FEM simulations of a single piezoelectric ZnO NS in contact with the cell membrane. (A) Model of a single ZnO NS, whose top end is free to move and is located at a distance of 5 nm from the membrane. The magnitudes of the electric field generated by the NS (x–z plane) and present at the cell membrane (x–y plane) for an ultrasound actuation at 3 MHz and 1.0 W cm^{-2} are depicted. (B) Model of a ZnO NS with top end embedded within the membrane. The magnitudes of the electric field generated by the single NS and present at the cell membrane under the same actuation conditions as (A) are also shown. (C) Zoom out of the 3D model showing how the ultrasound wave crosses the medium, modeled as an aqueous sphere. (D) Displacement of the NS actuated by the traveling ultrasound wave. E) Graphs comparing the magnitudes of the electric fields generated by the ZnO NS and present at the membrane in both models at the three intensities studied (0.2, 0.6, and 1.0 W cm^{-2}).

applied. Such versatility would allow the creation of customizable microdevices tailored for specific applications.

Despite this, the frequency of 3 MHz used for these experiments is far from the above 100 MHz resonance frequency values found in this simulation for a NS free to resonate. In a practical case, the free end of the NS would be in contact with the membrane through membrane biomolecules, lowering the final resonance frequency in one or two orders of magnitude. A parametric sweep for frequencies from 1 to 5 MHz was also performed to study how the frequency affected the electrical signal generated by the NS (Figure S8).

3 | Conclusion

In this work, wireless piezoelectric microdevices, smaller than a mammalian cell, were fabricated using scalable and highly reproducible microfabrication techniques. Millions of microdevices were obtained from a single silicon wafer, providing a low-cost fabrication solution. The μm-scale of the microdevice allows intimate contact with a single cell, while the nanometer-size of the ZnO NSs, grown on their surface, provides the piezoelectric functionality and allows making direct contact with the molecular structures of the cell membrane. The voltage generated by the piezoelectric ZnO NSs in the test device, when actuated by ultrasound at a frequency of 3 MHz, increased proportionally with the intensity of the ultrasound wave, producing an electric signal in the millivolt range.

Experiments using calcium-free medium, a VGCC blocker, and an SACC blocker demonstrated that piezoelectric ZnO NSs are able to induce an increase in intracellular calcium by triggering mainly extracellular calcium entry routes, through VGCCs and SACCs. The microdevices and the application of the ultrasound waves used to actuate them proved to be cytocompatible. The use

of ultrasound-actuated microdevices provokes a notable increase in the number of Saos-2 cells presenting calcium transients. The maximum percentage of excited cells was obtained with an ultrasound intensity of 1.0 W cm^{-2}. The total percentage of cells stimulated was 58%, nearly twice than in the control sample. Finally, FEM simulations indicated that a single NS actuated by ultrasound at 3 MHz and the three acoustic pressures used (0.2, 0.6, and 1.0 W cm^{-2}) can generate an electric field intensity in the range of 10^1 to 10^4 V cm^{-1}, depending on the cell-NS interaction, which is sufficient to trigger VGCCs, reinforcing the previous results.

While significant progress has been made, further research is warranted to fully elucidate the underlying mechanisms and optimize this approach for clinical translation. Taken together, the evidence presented highlights the promise of piezoelectric materials for cell stimulation and broader biomedical applications, including skin regeneration [3], fracture healing [16], chronic pain regulation [57], neuromodulation [13], cardiac peacemaking [4], and muscle stimulation [7].

4 | Experimental Section/Methods

4.1 | Microfabrication of the Microparticles

The overall process was developed in the microfabrication cleanroom at the IMB-CNM (CSIC), based on previous published works [37]. First, 4-inch silicon (Si) wafers were used as substrates and, after the corresponding cleaning, a layer of 1 ± 0.4 µm of silicon dioxide (SiO_2) was grown in the oven (TS Series V, Tempress) at a temperature of 1100°C. The following step was the deposition of aluminum nitride (AlN). The layer of AlN was sputtered (KS800HR, KENOSISTEC), reaching a thickness of 100 nm. Then, the photolithography step comprised the use of a positive photoresist (HiPR 6512) with a thickness of 1.2 µm. A reticle was used to define the micropatterns, consisting of an array of microparticles with an individual area of 3×3 μm^2, and a vertical and horizontal pitch of 3 µm. Afterwards, the etching of the 100 nm AlN layer was performed with a chlorinated mixture for 25 s (SI 500 ICP-RIE plasma etcher, SENTECH). The resist was annealed for 30 min at 200°C. Then, the SiO_2 layer beneath the metal was dry etched for 16 min (DIR-160, Alcatel) until the Si layer was reached (NanoSpec 6100, Nanospec). Finally, the Si layer was etched by isotropic reactive ion etching for 25 s (601E, Alcatel) to create the microparticle standing pillars, etching 0.8 µm per side. The resist was stripped after the etching. The microparticle standing pillars were checked through optical microscopy. In addition, the overall state of the wafer, specifically the homogeneity and the microparticle definition, was examined using SEM (Auriga-40, Carl Zeiss).

4.2 | Hydrothermal Growth of ZnO NSs

The wafers were diced into smaller pieces. These wafer pieces were placed upside down in a sealed container suitable for their size. Then, they were immersed in a $ZnNO_3 \cdot 6(H_2O)$:HMTA (2:1) solution and placed in an oven at 80°C for 9 h. These hydrothermal growth conditions allow ZnO NSs to grow on the wafer surface thanks to the catalytic effect of the AlN layer. After the chemical reaction took place, the wafer pieces were removed from the container. They were rinsed, first in deionized water and then in ethanol, for 1 min in each. Rinsing in ethanol prevented the collapse of the nanostructures due to its lower surface tension. Later, the wafer pieces were left to dry at room temperature and stored. At that point, the microdevices, still attached to the substrate wafer, have been created by combining the supporting microparticles and the integrated ZnO NSs.

A similar procedure was used to create microscopic glass coverslip samples covered with ZnO NSs. Coverslips of 12 mm diameter sputtered with a layer of 100 nm AlN were immersed in the $ZnNO_3 \cdot 6(H_2O)$:HMTA (2:1) solution and placed in an oven at 80°C for 9 h. The consecutive rinsing steps were also carried out for these samples.

The SEM inspection allowed us to characterize the morphology of the ZnO NSs. Parameters such as thickness, orientation and surface covering were measured for a magnification range from 100 to 50KX using the SE2 detector at 2 keV energy.

4.3 | Peeling off the Microdevices

The wafer pieces produced after the hydrothermal growth step were reduced to 1×1 cm^2 size chips. They were attached to a glass slide with double-sided tape and were covered completely covered with aqueous mounting medium (Fluoromount, Sigma-Aldrich). After drying overnight, the polymeric layer was peeled off, detaching the microdevices from the silicon substrate. Later, 1 mL of deionized water was added to dissolve the polymer for 3 h. Several washing steps were performed to remove the Fluoromount polymer, waiting 3 h after each washing step for the microdevices to precipitate. Finally, the microdevices were resuspended in ethanol to preserve them from contamination [37].

Before each experiment, the ethanol was removed, and the microdevices were resuspended in cell medium. The concentration of each batch was quantified in a Neubauer chamber.

4.4 | Electrical Characterization of the ZnO NS Piezoelectric Layer

The test devices used to evaluate the electrical performance of ZnO NSs included a glass coverslip covered by ZnO NSs. For this analysis, a bottom electrode was metallized with 100 nm of Mo, and later sputtered with 100 nm of AlN. The hydrothermal growth was carried out as described in the previous section. The upper electrode was fabricated by metallizing with 50 nm of Pt on a hydrofluoric acid (HF)-etched coverslip, presenting a rough surface. This rough surface, with a pseudo zig-zag profile, allowed the sweeping of the NSs' tips when the top electrode moves, for example, in response to ultrasound actuation. The whole test device was embedded in an epoxy resist (Araldite, Huntsman Advanced Materials) as an insulation barrier.

The setup was actuated with an ultrasound transducer (Sonic-Stimu Basic, Nu-Tek) at different intensities and a frequency of 3 MHz. The transducer tip was placed in direct contact

with the test device through a 6 mm-thick ultrasound hydrogel (GEL G008 ECO&IPL, FIAB), which served as the coupling medium and covered the entire interface between the equipment and the sample. The electrical response of the piezoelectric ZnO NS layer was measured with an oscilloscope (HMO3004, Rohde&Schwartz), with an input impedance of 1 MΩ. The whole setup is depicted in Figure S2.

The data was treated with a low-pass filter coded in MATLAB 2017b (MATLAB, MathWorks) to obtain a cleaner signal by removing the noise below 50 Hz.

4.5 | Cell Culture Experiments

Human osteosarcoma cells of the Saos-2 line (ATCC HTB 85) were cultured in Dulbecco's Modified Eagle's Medium (DMEM; Gibco) supplemented with 10% fetal bovine serum (FBS; Gibco) and under standard conditions (humidified air atmosphere with 5% CO_2, 37°C). Passage numbers ranged from p20 to p30.

For the viability experiments, 5×10^4 cells per well were seeded in a 4-well plate (Thermo Fisher) and were cultured for 24 h to allow cell adhesion on glass coverslips inserted in the wells. After that, 10×10^4 microdevices were added to each well. The proportion between microdevices and cells was 2:1. Samples were then evaluated after 1, 3, and 7 days. To assess the cytotoxic effect of the microdevices, a live/dead viability/cytotoxicity kit (Invitrogen) containing calcein AM (0.5 $\mu L mL^{-1}$) and ethidium homodimer-1 (2 $\mu L mL^{-1}$) was added. The culture plate was incubated at 37°C for 20 min in the dark and was then observed under an inverted fluorescence microscope (Olympus IX71 Inverted Fluorescence Microscope). Eight images from different fields were taken. Then, an ImageJ Cell Counter (NIH) was used to process the images.

SEM analysis was used to assess the position of the microdevices with respect to the cells. Samples were fixed with 4% paraformaldehyde (PFA) for 15 min and were dehydrated using increasing concentrations of ethanol (30%, 50%, 70%, 90%, 100%) for 15 min. After that, the samples were dried using hexamethyldisilazane (HMDS; Sigma-Aldrich) for 45 min. The magnification of the images ranged from 100 to 50KX at 2 keV.

4.6 | Effect of Ultrasound Actuation on Microdevice Integrity and Cell Viability

For the study of the cytotoxicity of ultrasound in Saos-2 cells, an ultrasound wave of 3 MHz frequency and different intensities (0.2, 0.6, and 1.0 W cm^{-2}) was applied. The stimulation was performed with an ultrasound transducer (Sonic-Stimu Basic, Nu-Tek). Ultrasound actuation was delivered for 10 s every 5 min, three consecutive times. The ultrasound transducer was placed in direct contact with the cell culture medium, positioned at a distance of around 1 cm from the cell layer. The setup used and a scheme of the protocol followed are depicted in Figure S4.

First, any possible damage or flaking in microdevices due to the effect of ultrasound was evaluated. For this, SEM images of three microdevice arrays were taken before and after the exposure to three cycles of 10 s of ultrasound actuation at 3 MHz and 1.0 W cm^{-2}. Surface morphology and detachment from the silicon substrate were studied (Figure S5).

The ultrasound intensity and frequency were optimized to be non-damaging for the cell and able to actuate the piezoelectric ZnO NSs. Frequencies of 1 and 3 MHz were evaluated to elucidate their effect on cytocompatibility (Movie S1 and Figure S6). To assess the cytotoxic effect of ultrasound after 24 h, a similar protocol using the live/dead staining kit as for the study of the cytotoxicity of the microdevices was used. The culture plate was also observed under an inverted fluorescence microscope (Olympus IX71 Inverted Fluorescence Microscope), taking eight images from different fields. ImageJ Cell Counter (NIH) was used to process the images.

Complementarily, temperature in the DMEM culture medium was measured during the application of ultrasound for the 10 s stimulation using a thermometer with a sensitivity of 0.1°C.

4.7 | Unravelling the Origin of Ca^{2+} from Intracellular Calcium Transients in Response to ZnO NSs Interaction

The origin of the Ca^{2+} from intracellular calcium transients, whether it is extracellular or intracellular, was studied. A total of 5×10^4 cells per well were seeded in a 4-well plate and cultured for 24 h to allow cell adhesion on glass coverslips, without (control) or with ZnO NSs. After, the samples were prepared for examination under the CLSM. Samples were washed with medium without FBS and incubated for 30 min at 37°C in the dark with medium without FBS containing 1 $\mu L mL^{-1}$ Fluo-4 calcium dye (Thermo Fisher Scientific). Once the incubation was completed, the medium was removed, and the cells were washed again with the medium without FBS.

Calcium-free conditions were induced by culturing the cells in calcium-free Hank's balanced salt solution (HBSS, Gibco). The coverslips were placed upside-down in a glass-bottom Petri dish with the cells facing the glass bottom. At the CLSM, tempered at 37°C, they were incubated in HBSS for 10 min. Images were taken from a single area for a total of 15 min. A 10X objective was used. Between 150 and 200 cells were studied for each condition. The time-lapse images were analyzed, and the number of cells presenting intracellular calcium transients was quantified using ImageJ ROI manager tool (NIH). Excited cells exhibited at least one event of fluorescence intensity exceeding a 5-fold increase over the basal signal during the 15-min time-lapse recording.

Nifedipine 1 μM, an L-type VGCC blocker, was used to locate the origin of the extracellular Ca^{2+} influx. After 24 h, the same Fluo-4 calcium dye protocol was applied to the samples. Coverslips were placed with the cells facing the glass bottom of the Petri dish, and samples were incubated at the CLSM in DMEM without FBS and without phenol red for 10 min and 37°C. Images were taken from a single area for 15 min. At minute 7, nifedipine 1 μM was applied to the sample while the time-lapse recording continued. A 10X objective was used. Between 100 and 150 cells were studied for each condition. A similar experiment was performed using gadolinium (Gadolinium (III) chloride hexahydrate, Merck) 50 μM, a non-specific SACC blocker. The

time-lapse images were analyzed, and the number of cells presenting intracellular calcium transients was quantified using ImageJ ROI manager tool (NIH). The number of excited cells was measured as described previously. The results on the number of cells producing intracellular calcium transients obtained from time-lapse images before and after the addition of each blocker were compared.

4.8 | Study of the Cell Transmembrane Potential in Response to the Interaction with ZnO NSs

Bis-(1,3-Dibutylbarbituric Acid)Trimethine Oxonol ($DiBAC_4(3)$, Thermo Fisher), a slow-response voltage-sensitive probe, was used to prove the voltage-dependent response of Saos-2 cells in contact with ZnO NSs. Similarly to the previous experiments, 5×10^4 cells per well were seeded on glass coverslips and cultured for 24 h to allow cell adhesion. Then, samples were washed and were incubated for 30 min at 37°C in the dark with medium without FBS and a concentration of 3 μM $DiBAC_4(3)$. The samples were washed again after the incubation and prepared for the CLSM examination at 37°C, the coverslips were placed with the cells adhered upside-down in a glass-bottom Petri dish. A time-lapse video from a single area was recorded for 20 min using a 10X objective. Between 100 and 150 cells were studied for each condition. The time-lapse images were analyzed both qualitatively and quantitatively using the ImageJ ROI manager tool (NIH).

4.9 | Ultrasound Actuation of Microdevices and Effect on Cell Stimulation

The calcium transients in Saos-2 cells cultured on top of the microdevices were studied to evaluate the electrical stimulation generated by the microdevices when ultrasound was applied. Ultrasound actuation at 3 MHz frequency and different intensities (0.2, 0.6, and 1.0 W cm^{-2}) was tested. The ultrasound transducer was placed in direct contact with the cell culture medium, positioned at a distance of around 1 cm from the cell layer. During the first 3 min of the time-lapse experiment, the basal cellular excitation level (without stimulus applied) was recorded. Then, ultrasound actuation (for 10 s) was applied and the effect on the calcium transients was recorded for the following 5 min. The same ultrasound actuation was applied repeatedly three times per sample. The procedure and setup can be checked in Figure S4.

All data from the replicates were acquired at the CLSM. Samples were prepared by seeding 5×10^4 cells per well in a 4-well plate and incubating them for 24 h on top of the microdevices. Control samples were seeded directly on top of glass-bottom Petri dishes. After 24 h of incubation, the samples were prepared for examination under the CLSM. Samples were washed with medium without FBS and were incubated for 30 min and at 37°C in the dark with medium without FBS and a concentration of 1 $\mu L mL^{-1}$ FLUO-4 calcium dye (Thermo Fisher Scientific). Once the incubation was completed, the medium was removed, and the cells were washed again with the medium without FBS. Finally, the microdevice arrays with cells seeded were placed in a glass-bottom Petri dish and were incubated in the medium without phenol red for 10 min at 37°C. Controls without microdevices were seeded directly on top of the glass-bottom Petri dish.

At the CLSM, tempered at 37°C, the sample was placed upside-down with the cells facing the glass bottom of the Petri dish. Images were taken from a single area for a total of 18 min. After each stimulation, the area was recorded for 5 min to capture the changes in calcium cell activity. The areas selected should contain a minimum of 45 cells. A 10X objective was used. Between 230 and 570 cells were studied for each condition. The time-lapse images were analyzed, and the number of cells with intracellular calcium transients was quantified. First, excited cells exhibiting at least one event of fluorescence intensity 5-fold higher than the basal signal during the 5-min recording after each stimulation were quantified. Subsequently, the cumulative response over the entire 18-min time-lapse was also quantified.

4.10 | FEM Simulations

COMSOL Multiphysics 6.0 (COMSOL, Sweden) 3D finite element software was used to simulate the electrical activity of a single ZnO NS interacting with the cell membrane when actuated with ultrasound. The stress produced by the ultrasound wave in the ZnO NS and the electric field created around the cell membrane were studied.

First, the dimensions of the ZnO NS were defined based on the measurements performed by SEM analysis. In the model, a ZnO NS is anchored to the microparticle, defining the bottom as a fixed constraint. In the first simulation, the upper edge of the ZnO NS is free to move, close to the cell membrane, at a distance of 5 nm. In the second simulation, the upper edge of the ZnO NS is embedded in the cell membrane, fixing the tip of the ZnO NS. The ZnO NS and the membrane modelled had a thickness of 30 nm and 10 nm, respectively. The whole system was embedded in a sphere of saline water. Other parameters, such as the relative permittivity (ε_r) of the cell membrane, were obtained from the literature [58].

Stationary and time-dependent studies were performed. From the stationary study, the data concerning the electric field produced by the ZnO NS using a 3 MHz frequency were extracted and are detailed in the FEM simulations section of 'Results'. A parametric sweep for frequency, ranging from 1 to 5 MHz, was also performed (Figure S8). All the studies were performed using an acoustic pressure of 0.2, 0.6, and 1.0 W cm^{-2}, following the same conditions as in the previous biological experiments performed with ultrasound. In the time-dependent study, the applied ultrasound frequency was also set to 3 MHz. In this study, we analyzed the behavior of the system from the beginning of the acoustic stimulus to the stationary phase (Movies S5). The ultrasound wave was coming from the bottom of the system (-z) at an angle of 45°.

Complementary to these studies, a parametric sweep of different sizes of the ZnO NSs was performed to obtain the resonance frequency of these nanostructures. The ZnO NS thicknesses in this study ranged from 15 to 40 nm, and the diameters ranged from 350 to 550 nm.

An anisotropic tetrahedral mesh was created to improve convergence and solver efficiency. The minimum element size in the mesh, in the NS-membrane system, was 10 nm. In the NS, it ranged from 10 to 30 nm, and in the cell membrane, up to 150 nm. The maximum element size, in the water sphere, was 58 μm, calculated to provide a good definition of the ultrasound wave ($\lambda/8$).

4.11 | Statistical Analysis

Statistical software (GraphPad, Prism 8.0.2) was used to conduct statistical analyses. The difference between the groups was obtained by performing chi-square tests for the results of the calcium imaging experiment, considering $p < 0.05$ (*) as the minimum statistical difference level. Student *t*-test was used to compare the percentages of cytocompatibility correlating ultrasound-actuated microdevices and microdevices without remote actuation. The same tests were used to evaluate the cytocompatibility for the different intensities of the ultrasound wave that were applied. The statistical significance considered in every test was $p < 0.05$ (*). All statistically analyzed biological experiments include at least three replicates.

Acknowledgements

L.L. would like to thank CSIC for the funding obtained through the JAE Intro 2019 and JAE Intro ICUs (BOE-A-2007-14853) programs. This work was carried out within the framework of the Ph.D. program in Biotechnology of the Universitat Autònoma de Barcelona (UAB). L.B. would like to acknowledge the Praemium Academiae grant (No. AP2202) provided by the Czech Academy of Sciences. A. B. received funding from a postdoctoral fellowship within the Beatriu de Pinós program, funded by the Secretary of Universities and Research (Government of Catalonia) and by the Horizon 2020 program of research and innovation of the European Union under Marie Sklodowska-Curie grant agreement No. 801370. G.M. thanks the La Caixa Foundation for the Junior Leader Retaining Fellowship program (LCF/BQ/ PR19/11700010) and MINECO for the Ramon y Cajal Fellowship (RYC2020-030501-I). This work was supported by the Agencia Estatal de Investigación from the Spanish Government (PID2023-148047OB-C21, and PID2023-148047OA-C22), and from the European Union under the Dynamization Actions Europa Excelencia 2020 funded by NextGenerationEU Instrument (EUR2020-112082, PIEZO2CELL). This work also received additional support from the Spanish State Research Agency, through the María de Maeztu Program for Units of Excellence in R&D (CEX2023-001397-M) and the Generalitat de Catalunya-AGAUR (2021 SGR 00497 and 2021-SGR-00122). Finally, the authors also want to acknowledge all the efforts of the staff at IMB-CNM (CSIC), especially the cleanroom engineers, and the staff of the Servei de Microscòpia de la Universitat Autònoma de Barcelona. The Z-potential characterization of the presented microdevices has been performed by the Unit 6 of the ICTS "NANBIOSIS", which is part of the CIBER in Bioengineering, Biomaterials & Nanomedicine (CIBER-BBN) at the Barcelona Materials Science Institute.

Conflicts of Interest

The authors declare no conflicts of interest.

Data Availability Statement

The data that support the findings of this study are available from the corresponding author upon reasonable request.

References

1. R. M. Neely, D. K. Piech, S. R. Santacruz, M. M. Maharbiz, and J. M. Carmena, "Recent Advances in Neural Dust: Toward a Neural Interface Platform," *Current Opinion in Neurobiology* 50 (2018): 64–71, https://doi.org/10.1016/j.conb.2017.12.010.

2. J. Shi, S. Kim, P. Li, et al., "Active Biointegrated Living Electronics for Managing Inflammation," *Science* 384 (2024): 1023–1030, https://doi.org/10.1126/science.adl1102.

3. H. Xue, J. Jin, Z. Tan, et al., "Flexible, Biodegradable Ultrasonic Wireless Electrotherapy Device Based on Highly Self-aligned Piezoelectric Biofilms," *Science Advances* 10 (2024): adn0260, https://doi.org/10.1126/sciadv.adn0260.

4. R. Qiu, X. Zhang, C. Song, et al., "E-cardiac Patch to Sense and Repair Infarcted Myocardium," *Nature Communications* 15 (2024): 4133, https://doi.org/10.1038/s41467-024-48468-x.

5. S. Waqar, L. Wang, and S. John, "Chapter 9 – Piezoelectric Energy Harvesting From Intelligent textiles," in *Electronic Textiles*, ed. T. Dias (Woodhead Publishing, 2015), 173–197, https://doi.org/10.1016/B978-0-08-100201-8.00010-2.

6. A. H. Rajabi, M. Jaffe, and T. L. Arinzeh, "Piezoelectric Materials for Tissue Regeneration: A Review," *Acta Biomaterialia* 24 (2015): 12–23, https://doi.org/10.1016/j.actbio.2015.07.010.

7. D. K. Piech, B. C. Johnson, K. Shen, et al., "A Wireless Millimetre-Scale Implantable Neural Stimulator With Ultrasonically Powered Bidirectional Communication," *Nature Biomedical Engineering* 4 (2020): 207–222, https://doi.org/10.1038/s41551-020-0518-9.

8. C. Shi, V. Andino-Pavlovsky, S. A. Lee, et al., "Application of a Sub–0.1-mm 3 Implantable Mote For In Vivo Real-Time Wireless Temperature Sensing," *Science Advances* 7 (2021): abf6312, https://doi.org/10.1126/sciadv.abf6312.

9. A. Marino, M. Battaglini, D. De Pasquale, A. Degl'Innocenti, and G. Ciofani, "Ultrasound-Activated Piezoelectric Nanoparticles Inhibit Proliferation of Breast Cancer Cells," *Scientific Reports* 8 (2018): 6257, https://doi.org/10.1038/s41598-018-24697-1.

10. C. Li, C. Xiao, L. Zhan, et al., "Wireless Electrical Stimulation at the Nanoscale Interface Induces Tumor Vascular Normalization," *Bioactive Materials* 18 (2022): 399–408, https://doi.org/10.1016/j.bioactmat.2022.03.027.

11. X. Meng, X. Xiao, S. Jeon, et al., "Self-contracting, Battery-free Triboelectric Wound Healing Strip With Strong Wet Adhesion," *Nature Communications* 16 (2025): 7220, https://doi.org/10.1038/s41467-025-62312-w.

12. X. Hou, J. Jing, Y. Jiang, et al., "Nanobubble-actuated Ultrasound Neuromodulation for Selectively Shaping Behavior in Mice," *Nature Communications* 15 (2024): 2253, https://doi.org/10.1038/s41467-024-46461-y.

13. C. H. Fan, H. C. Tsai, Y. S. Tsai, et al., "Selective Activation of Cells by Piezoelectric Molybdenum Disulfide Nanosheets With Focused Ultrasound," *ACS Nano* 17 (2023): 9140–9154, https://doi.org/10.1021/acsnano.2c12438.

14. G. Murillo, A. Blanquer, C. Vargas-estevez, et al., "Electromechanical Nanogenerator–Cell Interaction Modulates Cell Activity," *Advanced Materials* 29 (2017): 1605048, https://doi.org/10.1002/adma.201605048.

15. O. Careta, J. Fornell, E. Pellicer, et al., "Zno Nanosheet-coated Tizrpdsinb Alloy as a Piezoelectric Hybrid Material for Self-stimulating Orthopedic Implants," *Biomedicines* 9 (2021): 352, https://doi.org/10.3390/biomedicines9040352.

16. X. Cui, L. Xu, Y. Shan, et al., "Piezocatalytically-induced Controllable Mineralization Scaffold With Bone-Like Microenvironment to Achieve Endogenous Bone Regeneration," *Science Bulletin* 69 (2024): 1895–1908, https://doi.org/10.1016/j.scib.2024.04.002.

17. R. Mestre, J. Fuentes, L. Lefaix, et al., "Improved Performance of Biohybrid Muscle-Based Bio-Bots Doped With Piezoelectric Boron

Nitride Nanotubes," *Advanced Materials Technologies* 8 (2023): 2200505, https://doi.org/10.1002/admt.202200505.

18. A. Marino, S. Arai, Y. Hou, et al., "Piezoelectric Nanoparticle-Assisted Wireless Neuronal Stimulation," *ACS Nano* 9 (2015): 7678–7689, https://doi.org/10.1021/acsnano.5b03162.

19. G. S. Pitt, M. Matsui, and C. Cao, "Voltage-Gated Calcium Channels in Nonexcitable Tissues," *Annual Review of Physiology* 83 (2021): 183–203, https://doi.org/10.1146/annurev-physiol-031620-091043.

20. B. P. Bean, "The Action Potential in Mammalian Central Neurons," *Nature Reviews Neuroscience* 8 (2007): 451–465, https://doi.org/10.1038/nrn2148.

21. M. F. Schneider and C. W. Ward, "Initiation and Termination of Calcium Sparks in Skeletal Muscle," *Frontiers in Bioscience* 7 (2002): d1212–1222, https://doi.org/10.2741/A834.

22. L. Zhao, Z. Gao, W. Liu, et al., "Promoting Maturation and Contractile Function of Neonatal Rat Cardiomyocytes by Self-powered Implantable Triboelectric Nanogenerator," *Nano Energy* 103 (2022): 107798, https://doi.org/10.1016/j.nanoen.2022.107798.

23. M. E. Mycielska and M. B. A. Djamgoz, "Cellular Mechanisms of Direct-current Electric Field Effects: Galvanotaxis and Metastatic Disease," *Journal of Cell Science* 117 (2004): 1631–1639, https://doi.org/10.1242/jcs.01125.

24. B. Cortese, I. E. Palamà, S. D'Amone, and G. Gigli, "Influence of Electrotaxis on Cell Behaviour," *Integrative Biology* 6 (2014): 817–830, https://doi.org/10.1039/C4IB00142G.

25. N. Özkucur, T. K. Monsees, S. Perike, H. Q. Do, and R. H. W. Funk, "Local Calcium Elevation and Cell Elongation Initiate Guided Motility in Electrically Stimulated Osteoblast-Like Cells," *PLoS ONE* 4 (2009): 6131, https://doi.org/10.1371/journal.pone.0006131.

26. L. Khatib, D. E. Golan, and M. Cho, "Physiologic Electrical Stimulation Provokes Intracellular Calcium Increase Mediated by Phospholipase C Activation in human Osteoblasts," *The FASEB Journal* 18 (2004): 1903–1905, https://doi.org/10.1096/fj.04-1814fje.

27. R. H. W. Funk, T. K. Monsees, and N. Özkucur, "Electromagnetic Effects—From Cell Biology to Medicine," *Progress in Histochemistry and Cytochemistry* 43 (2009): 177–264, https://doi.org/10.1016/j.proghi.2008.07.001.

28. J. Li, L. Zhao, I. K. Ferries, et al., "Skeletal Phenotype of Mice With a Null Mutation in Cav 1.3 L-type Calcium Channel," *Journal of Musculoskeletal & Neuronal Interactions* 10 (2010): 180–187.

29. M. Uhlén, L. Fagerberg, B. M. Hallström, et al., "Tissue-based Map of the human Proteome," *Science* 347 (2015): 1260419, https://doi.org/10.1126/science.1260419.

30. A. Carter, K. Popowski, K. Cheng, A. Greenbaum, F. S. Ligler, and A. Moatti, "Enhancement of Bone Regeneration Through the Converse Piezoelectric Effect, a Novel Approach for Applying Mechanical Stimulation," *Bioelectricity* 3 (2021): 255–271, https://doi.org/10.1089/bioe.2021.0019.

31. F. Kao, P. Chiu, T. Tsai, and Z. Lin, "The Application of Nanogenerators and Piezoelectricity in Osteogenesis," *Science and Technology of Advanced Materials* 20 (2019): 1103–1117, https://doi.org/10.1080/14686996.2019.1693880.

32. F. Vasquez-Sancho, A. Abdollahi, D. Damjanovic, and G. Catalan, "Flexoelectricity in Bones," *Advanced Materials* 30 (2018): 1705316, https://doi.org/10.1002/adma.201705316.

33. V. K. Kaliannagounder, N. P. M. J. Raj, A. R. Unnithan, et al., "Remotely Controlled Self-powering Electrical Stimulators for Osteogenic Differentiation Using Bone Inspired Bioactive Piezoelectric Whitlockite Nanoparticles," *Nano Energy* 85 (2021): 105901, https://doi.org/10.1016/j.nanoen.2021.105901.

34. H. Lozano, G. Catalán, J. Esteve, N. Domingo, and G. Murillo, "Nonlinear Nanoscale Piezoresponse of Single ZnO Nanowires Affected by Piezotronic Effect," *Nanotechnology* 32 (2020): 025202, https://doi.org/10.1088/1361-6528/abb972.

35. G. Murillo, E. Leon-Salguero, P. R. Martínez-Alanis, J. Esteve, J. Alvarado-Rivera, and F. Güell, "Role of Aluminum and HMTA in the Hydrothermal Synthesis of Two- dimensional n-doped ZnO Nanosheets," *Nano Energy* 60 (2019): 817–826, https://doi.org/10.1016/j.nanoen.2019.04.017.

36. A. Blanquer, O. Careta, L. Anido-Varela, et al., "Biocompatibility and Electrical Stimulation of Skeletal and Smooth Muscle Cells Cultured on Piezoelectric Nanogenerators," *International Journal of Molecular Sciences* 23 (2022): 432, https://doi.org/10.3390/ijms23010432.

37. N. Torras, J. P. Agusil, P. Vázquez, et al., "Suspended Planar-Array Chips for Molecular Multiplexing at the Microscale," *Advanced Materials* 28 (2016): 1449–1454, https://doi.org/10.1002/adma.201504164.

38. J. Esteve i Tintó, J. A. Plaza, M. Duch Llobera, N. Torras Andrés, M. L. Perez García, and J. P. Agusil, "Método de Obtención de un Array de Micropartículas Planares con Multiplexado Molecular Superficial, Array Obtenido y Su uso Patent ES2555790B1," (2016), http://hdl.handle.net/10261/176295.

39. G. Murillo, I. Rodríguez-Ruiz, and J. Esteve, "Selective Area Growth of High-Quality ZnO Nanosheets Assisted by Patternable AlN Seed Layer for Wafer-Level Integration," *Crystal Growth & Design* 16 (2016): 5059–5066, https://doi.org/10.1021/acs.cgd.6b00661.

40. M. I. Arjona, M. Duch, A. Hernández-Pinto, et al., "Intracellular Mechanical Drugs Induce Cell-Cycle Altering and Cell Death," *Advanced Materials* 34 (2022): 2109581, https://doi.org/10.1002/adma.202109581.

41. G. Murillo, H. Lozano, J. Cases-Utrera, M. Lee, and J. Esteve, "Improving Morphological Quality and Uniformity of Hydrothermally Grown ZnO Nanowires by Surface Activation of Catalyst Layer," *Nanoscale Research Letters* 12 (2017): 51, https://doi.org/10.1186/s11671-017-1838-x.

42. L. Lefaix, M. Navarro, C. Nogués, A. Blanquer, and G. Murillo, "Tailoring Piezoelectric Nanogenerators and Microdevices for Cellular Excitation: Impact of Size and Morphology," *Advancement of Science* 12 (2025): 2415028, https://doi.org/10.1002/advs.202415028.

43. R. Gómez-Martínez, P. Vázquez, M. Duch, et al., "Intracellular Silicon Chips in Living Cells," *Small* 6 (2010): 499–502, https://doi.org/10.1002/smll.200901041.

44. T. Patiño, C. Nogués, E. Ibáñez, and L. Barrios, "Enhancing Microparticle Internalization by Nonphagocytic Cells Through the Use of Noncovalently Conjugated Polyethyleneimine," *International Journal of Nanomedicine* 7 (2012): 5671–5682, https://doi.org/10.2147/IJN.S34635.

45. Y. Chen, H. Ding, and S. Sun, "Preparation and Characterization of ZnO Nanoparticles Supported on Amorphous SiO_2," *Nanomaterials* 7 (2017): 217, https://doi.org/10.3390/nano7080217.

46. A. Carovac, F. Smajlovic, and D. Junuzovic, "Application of Ultrasound in Medicine," *Acta Informatica Medica* 19 (2011): 168–171, https://doi.org/10.5455/aim.2011.19.168-171.

47. C. A. Speed, "Therapeutic Ultrasound in Soft Tissue Lesions," *Rheumatology* 40 (2001): 1331–1336, https://doi.org/10.1093/rheumatology/40.12.1331.

48. R. Guldiken and O. Onen, "MEMS Ultrasonic Transducers for Biomedical Applications," in *MEMS for Biomedical Applications*, ed. S. Bhansali and A. Vasudev (Woodhead Publishing, 2012), 120–149, https://doi.org/10.1533/9780857096272.2.120.

49. U.S. Food and Drug Administration,"Marketing Clearance of Diagnostic Ultrasound Systems and Transducers: Guidance for Industry and FDA Staff," U.S. Department of Health and Human Services (2023).

50. K. R. Nightingale, C. C. Church, G. Harris, et al., "Conditionally Increased Acoustic Pressures in Nonfetal Diagnostic Ultrasound Examinations Without Contrast Agents: A Preliminary Assessment," *Journal of Ultrasound in Medicine* 34 (2015): 1–41, https://doi.org/10.7863/ultra.34.7.15.13.0001.

51. M. Kitsara, A. Blanquer, G. Murillo, et al., "Permanently hydrophilic, piezoelectric PVDF nanofibrous scaffolds promoting unaided electromechanical stimulation on osteoblasts," *Nanoscale* 11 (2019): 8906–8917, https://doi.org/10.1039/C8NR10384D.

52. H. Kito and S. Ohya, "Role of K^+ and Ca^{2+}-permeable Channels in Osteoblast Functions," *International Journal of Molecular Sciences* 22 (2021): 10459, https://doi.org/10.3390/ijms221910459.

53. A. Lacampagne, F. Gannier, J. Argibay, D. Garnier, and J. Y. Le Guennec, "The Stretch-activated Ion Channel Blocker Gadolinium Also Blocks L-type Calcium Channels in Isolated Ventricular Myocytes of the Guinea-Pig," *Biochimica et Biophysica Acta (BBA)-Biomembranes* 1191 (1994): 205–208, https://doi.org/10.1016/0005-2736(94)90250-x.

54. X. C. Zhang, K. Sun, L. Zhang, X. Li, and C. Cao, "GPCR Activation: Protonation and Membrane Potential," *Protein & Cell* 4 (2013): 747–760, https://doi.org/10.1007/s13238-013-3073-2.

55. M. J. Berridge, M. D. Bootman, and H. L. Roderick, "Calcium Signalling: Dynamics, Homeostasis and Remodelling," *Nature Reviews Molecular Cell Biology* 4 (2003): 517–529, https://doi.org/10.1038/nrm1155.

56. M. D. Bootman and G. Bultynck, "Fundamentals of Cellular Calcium Signaling: A Primer," *Cold Spring Harbor Perspectives in Biology* 12 (2020): a038802, https://doi.org/10.1101/cshperspect.a038802.

57. L. V. Borovikova, S. Ivanova, M. Zhang, et al., "Vagus Nerve Stimulation Attenuates the Systemic Inflammatory Response to Endotoxin," *Nature* 405 (2000): 458–462, https://doi.org/10.1038/35013070.

58. A. Chachaj-Brekiesz, J. Kobierski, A. Wnętrzak, and P. Dynarowicz-Latka, "Electrical Properties of Membrane Phospholipids in Langmuir Monolayers," *Membranes* 11 (2021): 53, https://doi.org/10.3390/membranes11010053.

Supporting Information

Additional supporting information can be found online in the Supporting Information section.

Supporting File 1: smll72834-sup-0001-SuppMat.docx.

Supporting File 2: smll72834-sup-0002-MovieS1.mp4.

Supporting File 3: smll72834-sup-0003-MovieS2.mp4.

Supporting File 4: smll72834-sup-0004-MovieS3.mp4.

Supporting File 5: smll72834-sup-0005-MovieS4.mp4.

Supporting File 6: smll72834-sup-0006-MovieS5.mp4.